

Modifying the Inter-Phase Drag via Solid Volume Fraction Gradient for CFD Simulation of Fast Fluidized Beds

Mingze Su

State Key Laboratory of Coal Combustion, School of Energy and Power Engineering, Huazhong University of Science and Technology, Wuhan 430074, P.R. China

Key Laboratory for Flow & Enhanced Heat Transfer of Shandong Academy of Sciences, Jinan 250014, P.R. China

Haibo Zhao

State Key Laboratory of Coal Combustion, School of Energy and Power Engineering, Huazhong University of Science and Technology, Wuhan 430074, P.R. China

DOI 10.1002/aic.15573

Published online February 1, 2017 in Wiley Online Library (wileyonlinelibrary.com)

The conventional drag model in two-fluid simulation, which assumes uniform particle distribution in a computational grid, overestimates the drag force, thus failed in capturing the subgrid-scale strands and resolvable-scale clusters. This work proposed a new modification to the conventional drag model through considering the heterogeneous distribution of solid volume fraction (SVF), especially, in the inter-phase boundary (i.e., cluster boundary). The resulting drag model is a function of particle Reynolds number, SVF and the gradient of SVF. This straightforward modification is consistent with the elaborately filtered-approach-based modification method in nature. A CFD simulation for a two-dimensional riser was conducted to validate the new drag model. The outlet solid mass flux, axial and radial time-averaged voidages from the new drag model agreed well with the experimental measurements, and these results were far better than those from the conventional homogeneous drag models. © 2017 American Institute of Chemical Engineers AIChE J, 63: 2588–2598, 2017
 Keywords: fast fluidization, drag coefficient, cluster, CFD simulation

Introduction

Most gas–solid two-phase flows in chemical engineering processes, such as fluid catalytic cracking, circulating fluidized bed combustion, and chemical looping combustion in interconnected fluidized bed reactor, are essentially nonlinear and nonequilibrium with the so-called multi-scale structure as their common nature.¹ In a fast fluidized bed with a complex flow behavior of gas and particle phases, gas–particle interaction is more intensive due to higher superficial velocity and solid mass flux, resulting in heterogeneous structure characterized by subgrid-scale strands, resolvable-scale clusters and a reactor-scale dilute-top/dense-bottom and dilute-core/dense-wall phenomenon.

The task of modeling the heterogeneous gas–solid flow structure in a fast-fluidized bed is still very challenging. Currently, there are two numerical techniques used for simulating fluidized beds, which are distinguished among the Eulerian–Lagrangian model with the Lagrangian trajectory tracking of single particle or a particle parcel (simulation particle), and the Eulerian–Eulerian model with the Eulerian description of dispersed phase as quasi-continuum phase.² The latter, namely the two-fluid model (TFM), was widely accepted in fluidized bed simulation because it can provide almost all details of multiphase flows within an

acceptable computational cost. An interpenetrating continuum assumption was applied in the TFM so that both the gas and particle phases can be treated as a continuum phase. The Newtonian form constitutive correlations were adopted for both the gas and particle phases. By the aid of the kinetic theory of granular flow which was originated from the theory for the nonuniform dense gases described by Chapman and Cowling,³ the so-called particle pressure and particle viscosity can be obtained.^{4,5}

The description to momentum exchange between the gas phase and the particle phase, i.e., the so-called gas–particle drag law, is a key model for the multiphase CFD (computational fluid dynamics) simulation of fluidized bed systems. In the past few years, many closures for drag law have been proposed from theoretical, experimental, and computational perspectives. Theoretical closures^{6,7} were limited to small solid volume fraction (SVF) and low Reynolds number. The widely-used correlation in chemical engineering, the Gidaspow model,⁵ which is a combination of the Wen & Yu model⁸ and the Ergun equation,⁹ was originally derived from the experimental results of homogeneous systems. Van der Hoef and his co-workers^{10,11} proposed several correlations based on Lattice Boltzmann simulation results for particle configuration of random arrays. However, the flow structure was definitely heterogeneous in gas–solid fluidization systems. The tendency of particles aggregating while interacting with gas has been validated by experiments. Therefore, the validity of adopting

Correspondence concerning this article should be addressed to H. Zhao at hzhao@mail.hust.edu.cn.

these homogeneous based drag correlations in heterogeneous gas–solid systems is quite questionable.

In fact, Li et al.¹² pointed out that the drag correlations derived from the homogeneous systems were inadequate to represent the gas–solid interaction in CFB systems. They also demonstrated significant dependence of drag coefficient on structural changes.¹³ O'Brien and Syamlal¹⁴ found that the drag correlations need to be corrected to account for cluster formation, and claimed that the unphysical adjustment to the solid stress was not correct. Qi et al.¹⁵ claimed that the current drag correlations were only suitable for low gas velocity and coarse particles. Agrawal et al.¹⁶ concluded that the failure of the conventional drag models in coarse grid simulations of fluidized beds is ascribed to not considering the effect of meso-scale structures (which are derived from an inertial instability mechanism associated with the relative motion between the gas and particle phases, and an instability mechanism due to damping of the fluctuating motion of particles by the interstitial fluid and inelastic collisions between particles).

Recently, some heterogeneous-structure-based drag models were proposed based on the energy minimization multi-scale (EMMS) principle.¹⁷ Among these, Yang et al.¹⁸ first proposed a heterogeneous drag correlation for CFD simulation of a riser. Depending on some actual and estimated experimental parameters, the correction factor of the EMMS-based heterogeneous drag coefficient to the standard drag coefficient can be obtained through a nonlinear programming process. In actual CFD simulation processes, the correction factor was only adopted in the dilute phase (the SVF $\phi < 0.26$) while the Ergun equation was still adopted in the dense phase. The critical voidage was determined as 0.74. The simulation result showed that the EMMS-based drag model can indeed improve simulation accuracy for the nonlinear process in the riser in comparison with the conventional homogeneous drag model. Afterwards, Wang et al.¹⁹ improved the EMMS-based drag model by adopting a revised cluster diameter correlation, which considered the added mass force in heterogeneous gas–solid flows. Lu et al.²⁰ considered that the correction factor for drag coefficient was related to the voidage but also the Reynolds number. A bivariate correction factor was proposed to simulate the same riser configuration as Yang et al.¹⁸ and Wang et al.¹⁹. The simulation results were in good agreement with the experimental results, indicating that the bivariate correction factor is able to improve substantially the model forecasting ability. Recently, Wang et al.²¹ proposed a cluster structure-dependent (CSD) drag model, which was successfully integrated in the two-fluid based CFD simulation. Different from previous works, the CSD drag model was a grid-based model rather than a reactor-based model. In other words, the CSD drag was calculated according to the local parameters in every computational grid and at every time step. However, computational cost may be unacceptable using the CSD drag model in simulation of actual engineering facility.

The EMMS principle has been widely accepted for CFD simulation of fluidized beds. However, the EMMS-based drag models need further development in, at least, two aspects. First, in EMMS-based CFD simulations, the combination of the EMMS drag coefficient and the Ergun equation was adopted, and the critical voidage (or SVF) which determines the selection of the drag laws was set artificially. The artificial critical voidage does not conform to the good physical base of the EMMS principle. Second, the reactor-based EMMS drag model, e.g., the Yang et al. model, can only be used in a

specified riser and in a specified operation condition, because the parameters used to determine the drag correlation are involved in the reactor geometric size and the operating parameters. The no-universality of these drag models limited their application. While the grid-based EMMS drag model (e.g., CSD model) is quite complicated, and can hardly be used in a CFD simulation for a real fluidized bed due to the limitation of computational cost.

Besides the EMMS-based modification, researchers attempted to study the drag modification in other ways. Igci et al.²² first constructed the filtered two fluid model equations, which reflected the influence of the subgrid-scale structures (i.e., strands) to the inter-phase drag force. This work presented a new approach to construct the filtered drag coefficient for considering the subgrid-scale strands (which is hardly captured by the conventional homogeneous drag model if the grid size is not highly resolved²³). Recently, Parmentier et al.²⁴ attempted to construct a new filtered drag correlation through utilizing highly-resolved TFM simulation results. The dimensionless SVF and filter size were taken as independent variables in the modification. These efforts demonstrated that the filtered drag modification provides a promising approach for modeling the heterogeneous gas–solid two-phase flows.

Generally speaking, most of the existent gas–solid inter-phase drag models were functions of voidage and Reynolds number, while the rest is also dependent on the filter size. However, the pre-specified voidage and Reynolds number cannot determine the drag force adequately, due to the heterogeneous subgrid-scale strands and resolvable-scale clusters, or saying, the variety of SVF distribution in the computational grids. The objective of the present work was to develop a solid volume fraction gradient-modified (SVFGM) drag model through theoretical analysis. Here, the drag force was determined simultaneously by three independent variables: particle Reynolds number, SVF and the gradient of SVF. A two-dimensional riser was simulated by adopting the present drag model and the homogeneous model for validating the reliability of the SVFGM drag model.

Description to the Model

Inspiration

As Agrawal et al.¹⁶ stated, the subgrid strand structures are formed as a result of the instability of gas–solid flows, leading to the decrease of the inter-phase drag force in a computational grid. It is deduced that the decrease of the interphase drag force will change flow pattern and lead to the appearance of the resolvable-scale clusters. (Here, the concepts of the subgrid-scale strand and the resolvable-scale cluster were distinguished.) The influence of the subgrid strands will not be remarkable any more inside the cluster region and the dilute region. However, in the cluster boundary, the appearance of subgrid strands will evidently reduce the interphase drag force, which factually maintains the cluster structure. The conventional homogeneous drag model fails to predict gas–particle flows because the subgrid heterogeneous structures are not captured. In other words, there is no mechanism to maintain the cluster structure in modeling. The closure relations proposed by Igci et al.²² and Parmentier et al.²⁴ succeeded in offering a self-maintained mechanism for the cluster structure through considering the subgrid strand effect in the filtered drag modifications. Inspired by the phenomenological

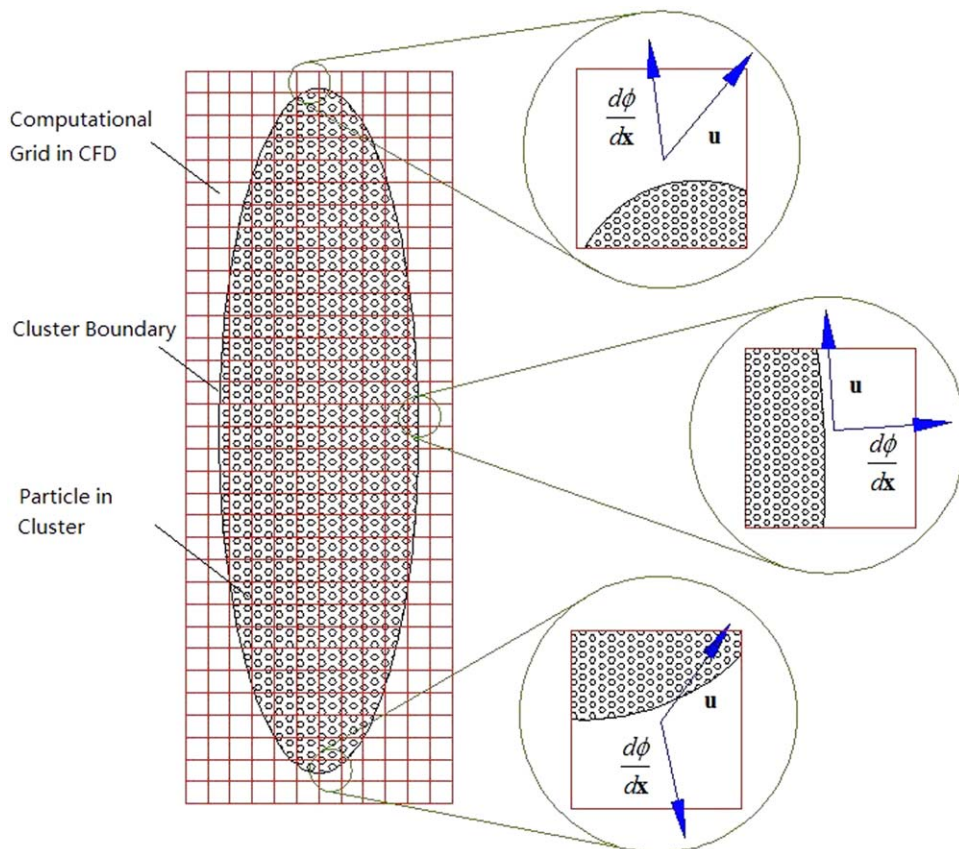


Figure 1. Schematic of the SVFGM drag model in CFD simulation process.

[Color figure can be viewed at wileyonlinelibrary.com]

Smagorinsky subgrid model²⁵ in large-eddy simulation of turbulent flow for single-phase fluid, we intended to introduce a gradient variable to construct a new drag modification which can offer the self-maintained mechanism for the cluster structure, rather than capturing these subgrid strand structures. The SVF gradient, which can reflect the effects of the SVF and the filter size, was adopted in our modification.

As mentioned above, there exists large heterogeneity in the cluster boundary grids and this heterogeneity can be characterized by the gradient of SVF. The boundary grids consist of dilute phase and dense phase simultaneously. For simplicity, take one dimensional grid for an example to illuminate the heterogeneous SVF distribution. The SVF distribution (ϕ) in a computational grid can be viewed as a smooth function taking the location (x) as variable, expressed as $\phi(x)$. The Taylor expansion of $\phi(x)$ is $\phi(x) = \phi_0 + a_1\Delta x + a_2\Delta x^2 + \dots$. If taking the first term only, the expansion reduces to $\phi(x) = \phi_0$, meaning that the heterogeneous SVF distribution in the boundary grid is represented by a homogeneous mean SVF. At this point, the dimensionless drag force is expressed as $F = F(\text{Re}, \phi_0)$. That is, the above expression corresponds to the conventional homogeneous drag model. If one takes the first two terms in the Taylor expansion, $\phi(x)$ can be expressed as $\phi(x) = \phi_0 + a_1\Delta x$, and the SVF distribution in a boundary grid is then characterized by two independent variables ϕ_0 and a_1 , where $a_1 = \frac{d\phi}{dx}$. Now the dimensionless drag force can be expressed as $F = F(\text{Re}, \phi_0, \frac{d\phi}{dx})$. The advantage of this drag model is that $\frac{d\phi}{dx}$ can be easily calculated in CFD

simulation by the finite difference method, which does not burden the computation greatly.

Model assumption

(1) **The direction of the SVF gradient is perpendicular to the gas velocity direction.** In fast fluidized beds, most of the gas will pass by the cluster instead of passing through it, as clearly observed in CFD simulations and experimental measurements.^{2,16,26} It indicates that the direction of gas phase velocity will be self-adjusted to fit the cluster boundary. Generally, on the cluster boundary the gas velocity direction will be perpendicular to the direction of the SVF gradient. Certainly, we agreed that the angle between the above two directions may not be strictly equal to 90° , especially on the top and bottom points of a cluster, as illuminated in Figure 1. However, we argued here that in most computational grids this deviation is not too significant.

(2) **The computational grid can be divided into a dense part and a dilute part. There is no mass exchange between the two parts.** As discussed above, the heterogeneous SVF function $\phi(x)$ is represented as $\phi(x) = \phi_0 + \frac{d\phi}{dx}\Delta x$ with the first-order accuracy. In practice, it is considered that the SVF gradient $\frac{d\phi}{dx}$ can be expressed as the difference between a higher SVF in the dense part and a lower SVF in the dilute part in a cell. There is no need to divide the grid into more parts (corresponding to take higher order terms of the Taylor expansion of $\phi(x)$) because this modification to the drag is only with the first-order accuracy. It is believed that there exists mass

exchange between the dense part and the dilute part in nature. However, the cluster size is greater than the grid size, and the flow around a cluster will undergo a developing and self-adjusting process. We argued here that the effect of mass exchange is negligible in the cluster boundary grids in fully developed flow regions. The assumption can be understood in the following ways: if there exists significant mass exchange in one grid due to pressure difference between the two parts, the pressure difference in next grid will decrease accordingly owing to the mass exchange in such grid. Along with the flow development, the negligible difference will gradually reach and this assumption of no mass exchange will become reasonable. One corollary of this assumption is that the total drag force acting on the particles in the dense part is equal to that in the dilute part.

Model implementation

Recently, Tang et al.¹¹ investigated the drag force in flow past static mono-disperse arrays of spheres through the immersed boundary method. Based on the simulation results, a new drag correlation with an average relative deviation of 4%, was proposed, which extends previously similar correlations to a wider range of SVF and Reynolds number. In this study, the Tang et al. model was taken as a foundation to be modified for describing the heterogeneous inter-phase interaction in the fast-fluidized beds. The dimensionless drag correlation of Tang et al. was expressed as¹¹:

$$F_T(\phi, \text{Re}) = \frac{10\phi}{(1-\phi)^2} + (1-\phi)^2(1+1.5\sqrt{\phi}) + \left[0.11\phi(1+\phi) - \frac{0.00456}{(1-\phi)^4} + (0.169(1-\phi) + \frac{0.0644}{(1-\phi)^4})\text{Re}^{-0.343} \right] \text{Re} \quad (1)$$

Then, the SVFGM drag coefficient can be calculated in CFD simulation by the following steps:

1. The SVF (ϕ_0) in each computational grid at each time step can be obtained in CFD simulation, then the SVF gradient ($\frac{d\phi}{dx}$) can be calculated through a differential process: for a

two-dimensional simulation, $\frac{d\phi}{dx} = \sqrt{\left(\frac{\phi_{j+1}-\phi_{j-1}}{2\Delta x}\right)^2 + \left(\frac{\phi_{j+1}-\phi_{j-1}}{2\Delta y}\right)^2}$.

2. The difference of the SVF between the dense part and the dilute part ($\Delta\phi = \phi_2 - \phi_1$) can be calculated by multiplying $\frac{d\phi}{dx}$ and the grid characteristic size.

3. Then the SVF in the dense part (ϕ_2) and in the dilute part (ϕ_1) can be calculated according to $\phi_1 = \phi_0 - \Delta\phi/2$ and $\phi_2 = \phi_0 + \Delta\phi/2$.

4. From assumption (2), the total drag force acting on the particles in the dense part is equal to that in the dilute part. Then the Reynolds number in the dense part (Re_2) and in the dilute part (Re_1) can be calculated as following

$$\text{Re}_1 + \text{Re}_2 = 2\text{Re} \quad (2)$$

$$F_{T1}(\phi_1, \text{Re}_1)\phi_1\text{Re}_1 = F_{T2}(\phi_2, \text{Re}_2)\phi_2\text{Re}_2 \quad (3)$$

where Re represents to the averaged Reynolds number, $F_{Ti}(\phi_i, \text{Re}_i)$ represents to the dimensionless drag force calculated from the Tang et al. model.

5. The total dimensionless drag force in a grid and the inter-phase drag coefficient which can be adopted in CFD simulation can be expressed as, respectively

$$F = \frac{F_{T1}\phi_1\text{Re}_1 + F_{T2}\phi_2\text{Re}_2}{2\phi_0\text{Re}} \quad (4.1)$$

$$\beta = \frac{18\mu_g\phi(1-\phi)}{d_p^2} F \quad (4.2)$$

Results and Discussion

Compatibility analysis with the filtered approach

Starting from the kinetic theory based TFM for gas particle flows, Igci et al.²² first constructed the filtered two fluid model equations that averaged over small scale in homogeneities, thus proposed the filtered approach for dealing with the drag modification. According to the filtered approach, the filtered variables were defined as follows²²:

$$\bar{\phi}(\mathbf{x}, t) = \int_V G(\mathbf{x}, \mathbf{y})\phi(\mathbf{y}, t)d\mathbf{y} \quad (5)$$

$$\bar{\phi}(\mathbf{x}, t)\bar{\mathbf{u}}_s(\mathbf{x}, t) = \int_V G(\mathbf{x}, \mathbf{y})\phi(\mathbf{y}, t)\mathbf{u}_s(\mathbf{y}, t)d\mathbf{y} \quad (6)$$

$$(1-\bar{\phi}(\mathbf{x}, t))\bar{\mathbf{u}}_g(\mathbf{x}, t) = \int_V G(\mathbf{x}, \mathbf{y})(1-\phi(\mathbf{y}, t))\mathbf{u}_g(\mathbf{y}, t)d\mathbf{y} \quad (7)$$

where $G(\mathbf{x}, \mathbf{y})$ is a weight function that acts as a space filter together with the volume integration; The weight function satisfies $\int_V G(\mathbf{x}, \mathbf{y})d\mathbf{y} = 1$; V denotes the region over which the gas-particle flow occurs. \mathbf{u} denotes the velocity for each phase; the subscript g and s represent the gas and solid phases, respectively; $\bar{\phi}(\mathbf{x}, t)$, $\bar{\mathbf{u}}_s(\mathbf{x}, t)$, $\bar{\mathbf{u}}_g(\mathbf{x}, t)$ are the filtered particle volume fraction, filtered velocities of solid and gas phases, respectively.

And the fluctuating variables were defined as²²:

$$\phi'(\mathbf{x}, t) = \phi(\mathbf{x}, t) - \bar{\phi}(\mathbf{x}, t) \quad (8)$$

$$\mathbf{u}'_s(x, t) = \mathbf{u}_s(x, t) - \bar{\mathbf{u}}_s(x, t) \quad (9)$$

$$\mathbf{u}'_g(x, t) = \mathbf{u}_g(x, t) - \bar{\mathbf{u}}_g(x, t) \quad (10)$$

where the superscript ' represents the fluctuating variables.

Applying the filtered approach to the continuity equations and the momentum balance equations in the two-fluid model, the filtered equations can be obtained as below²²:

$$\frac{\partial(\rho_g(1-\bar{\phi}))}{\partial t} + \nabla \cdot (\rho_g(1-\bar{\phi})\bar{\mathbf{u}}_g) = 0 \quad (11)$$

$$\frac{\partial(\rho_s\bar{\phi})}{\partial t} + \nabla \cdot (\rho_s\bar{\phi}\bar{\mathbf{u}}_s) = 0 \quad (12)$$

$$\frac{\partial(\rho_g(1-\bar{\phi})\bar{\mathbf{u}}_g)}{\partial t} + \nabla \cdot (\rho_g(1-\bar{\phi})\bar{\mathbf{u}}_g\bar{\mathbf{u}}_g) = -\nabla \cdot (\rho_g(1-\phi)\mathbf{u}'_g\mathbf{u}'_g - (1-\bar{\phi})\nabla \cdot \bar{\boldsymbol{\sigma}}_g - \bar{\mathbf{F}} + \rho_g(1-\bar{\phi})\mathbf{g}) \quad (13)$$

$$\frac{\partial(\rho_s\bar{\phi}\bar{\mathbf{u}}_s)}{\partial t} + \nabla \cdot (\rho_s\bar{\phi}\bar{\mathbf{u}}_s\bar{\mathbf{u}}_s) = -\nabla \cdot (\bar{\boldsymbol{\sigma}}_s + \rho_s\bar{\phi}\mathbf{u}'_s\mathbf{u}'_s + \bar{\phi}\nabla \cdot \bar{\boldsymbol{\sigma}}_g + \bar{\mathbf{F}} + \rho_s\bar{\phi}\mathbf{g}) \quad (14)$$

where ρ and $\boldsymbol{\sigma}_g$ represent the density and the stress-strain tensor for each phase, respectively. The filtered gas-particle interaction force is expressed as²²:

$$\bar{\mathbf{F}} = \bar{\mathbf{f}} - \overline{\phi' \nabla \cdot \sigma'_g} \quad (15)$$

Here $\bar{\mathbf{F}}$ consists of a filtered gas–particle drag force $\bar{\mathbf{f}}$ and a term representing correlated fluctuations in the particle volume fraction ϕ and the gas phase stress gradient $\nabla \cdot \sigma'_g$. The sub-grid structure effect was included in the second term on the right-hand side of Eq. 15.

Another filtered drag correlation proposed by Parmentier et al.²⁴, which is based on the highly resolved TFM simulation results, is dependent of the SVF and the dimensionless filter size ($\bar{\Delta}^*$):

$$\bar{\mathbf{F}} = \bar{\mathbf{f}}(1 - f(\bar{\Delta}^*)h(\bar{\phi})K_{\alpha\alpha}) \quad (16)$$

where $f(x)$ and $h(x)$ are the specific functions determined by the highly resolved TFM simulation results. $K_{\alpha\alpha}$ is a dynamically-adjusted constant.

Comparing Eq. 15 with Eq. 16, ones see that the modification given by Parmentier et al. can be factually expressed as:

$$\overline{\phi' \nabla \cdot \sigma'_g} = (f(\bar{\Delta}^*)h(\bar{\phi})K_{\alpha\alpha})\bar{\mathbf{f}} \quad (17)$$

Essentially, the decrease of the drag force due to the subgrid heterogeneous structures was modeled as the homogenous inter-phase drag force ($\bar{\mathbf{f}}$) multiplying a correlation factor (less than 1), and the factor is the function of dimensionless filter size ($\bar{\Delta}^*$) and the filtered (or, averaged) SVF ($\bar{\phi}$).

By far, the correction factor can be defined as:

$$\omega = (1 - f(\bar{\Delta}^*)h(\bar{\phi})K_{\alpha\alpha}) = \bar{\mathbf{F}}/\bar{\mathbf{f}} \quad (18)$$

Based on the definition in Eq. 18, the correction factor in our drag modification model can be calculated as the ratio of the modified inter-phase drag force F (in Eq. 4.1) to the homogeneous inter-phase drag force F_T (in Eq. 1). As shown in Figure 2, the correction factor was expressed as a function of ϕ , Re and $\frac{d\phi}{dx}$. As seen, the correction factor ω , which is nearly independent of Re , decreases as $\frac{d\phi}{dx}$ increases. For a smaller ϕ , ω decreases more quickly. ω is always lower than 1, indicating that the cluster formation results in the decrease of inter-phase drag force. The contour map of the correction factor for a fixed Re ($Re = 15$) was showed in Figure 3. When $\frac{d\phi}{dx} = 0$, the SVFGM model reduces itself to the Tang et al. model. On this condition, the correction factor was always equal to 1. Otherwise, as $\frac{d\phi}{dx}$ increases, ω decreases quickly. Factually, from Eq. 17 and Eq. 18 it can be found that a higher SVF gradient (a larger $\frac{d\phi}{dx}$) leads to a smaller

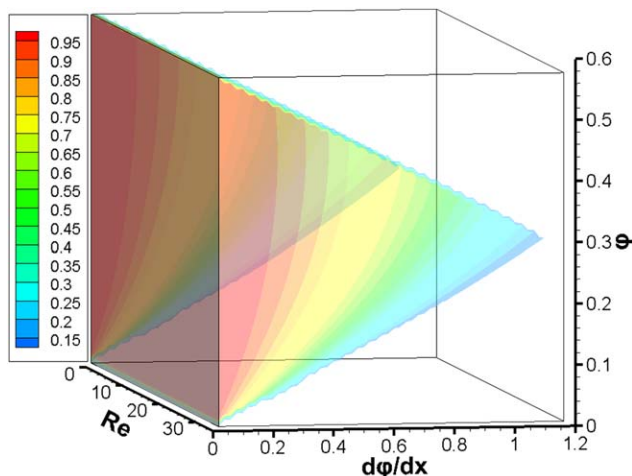


Figure 2. Iso-surface of the correction factor relative to Tang et al. model.

[Color figure can be viewed at wileyonlinelibrary.com]

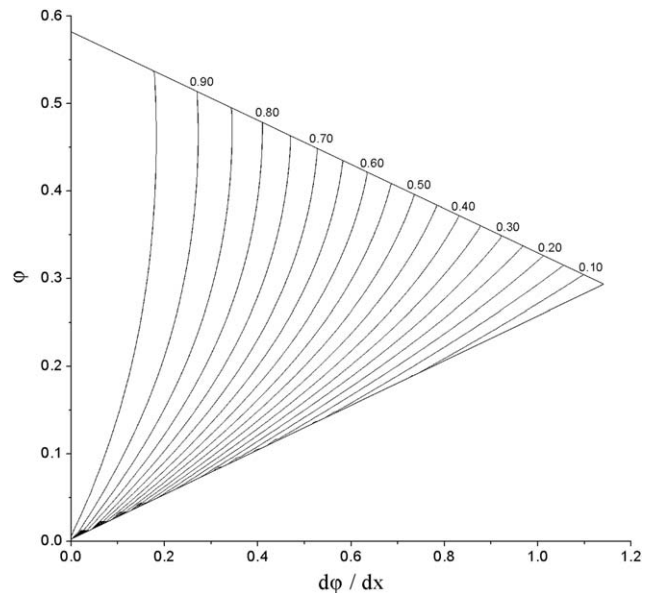


Figure 3. The correction factor as a function of $\frac{d\phi}{dx}$ and ϕ when $Re = 15$.

filtered drag force (i.e., a smaller ω). The analysis illustrated the present modification conforms to the filtered approach, and the modification based on SVF gradient can be seen as a kind of implementation method of the filtered approach.

Figure 4 shows a complicated relationship between the SVFGM model and the Gidaspow model. Obviously, there exist large differences between the SVFGM model and the Gidaspow model. In a similar way, the correction factor decreases as $\frac{d\phi}{dx}$ increases, and $\omega(\phi, Re, \frac{d\phi}{dx})$ decreases more quickly for a lower Re . The iso-surfaces were discontinuous due to the discontinuity of the Gidaspow model (the Wen & Yu model was adopted when the voidage is greater than 0.8, otherwise the Ergun equation was adopted).

Governing equations

All the equations in the hydrodynamic model of multiphase flow used in this study were listed in Table 1. The model

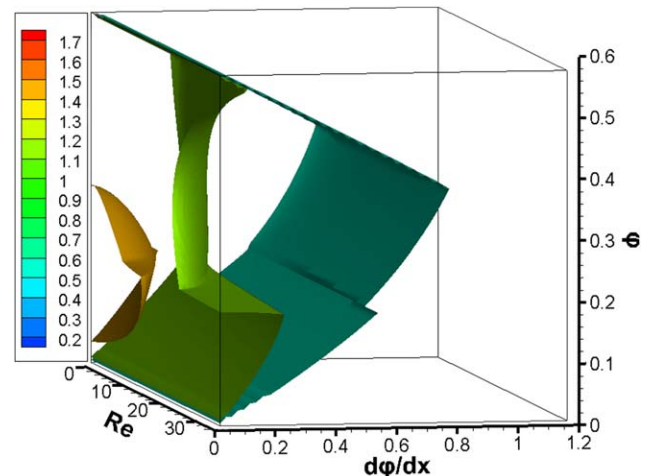


Figure 4. Iso-surface of the correction factor relative to Gidaspow model.

[Color figure can be viewed at wileyonlinelibrary.com]

Table 1. Governing Equations and the Relations in the Model (Filtered-Based)

Continuity equations	
$\frac{\partial(\alpha\rho)_g}{\partial t} + \nabla \cdot (\alpha\rho\mathbf{u})_g = 0$	(19)
$\frac{\partial(\alpha\rho)_s}{\partial t} + \nabla \cdot (\alpha\rho\mathbf{u})_s = 0$	(20)
Momentum equations	
$\frac{\partial(\alpha\rho\mathbf{u})_g}{\partial t} + \nabla \cdot (\alpha\rho\mathbf{u}^2)_g = -\alpha_g \nabla p + \alpha_g \rho_g \mathbf{g} + \nabla \cdot \boldsymbol{\sigma}_g - \beta(\mathbf{u}_g - \mathbf{u}_s)$	(21)
$\frac{\partial(\alpha\rho\mathbf{u})_s}{\partial t} + \nabla \cdot (\alpha\rho\mathbf{u}^2)_s = -\alpha_s \nabla p + \alpha_s \rho_s \mathbf{g} - \nabla P_s + \nabla \cdot \boldsymbol{\sigma}_s + \beta(\mathbf{u}_g - \mathbf{u}_s)$	(22)
Constitutive equations and other relational expressions	
$\boldsymbol{\sigma}_i = \alpha_i \mu_i (\nabla u_i + (\nabla u_i)^T) + \alpha_i (\zeta_i - \frac{2}{3} \mu_i) (\nabla \cdot u_i) \mathbf{I}$	(23)
$\mu_s = \frac{4}{3} \alpha_s \rho_s d_s G_0 (1+e) \sqrt{\frac{\Theta_s}{\pi} + \frac{10 \rho_s d_s \sqrt{\pi} \Theta_s}{96 \alpha_s G_0 (1+e)}} [1 + \frac{4}{3} \alpha_s G_0 (1+e)]^2 + \frac{P_s \sin \phi}{2 \sqrt{I_{2D}}}$	(24)
$\zeta_s = \frac{4}{3} \alpha_s \rho_s d_s G_0 (1+e) \sqrt{\frac{\Theta_s}{\pi}}$	(25)
$P_s = [1 + 2(1+e) \alpha_s G_0] \alpha_s \rho_s \Theta_s$	(26)
$\frac{\partial(\alpha_s \rho_s \Theta_s)}{\partial t} + \nabla \cdot (\alpha_s \rho_s \mathbf{u}_s \Theta_s) = \frac{2}{3} [- (P_s \mathbf{I} + \boldsymbol{\sigma}_s) : \nabla \mathbf{u}_s - \nabla \cdot (k_{\Theta_s} \nabla \Theta_s) - \gamma_{\Theta_s} + \phi_{\Theta_s}]$	(27)
$k_{\Theta_s} = \frac{15 \rho_s d_s \alpha_s \sqrt{\Theta_s \pi}}{4(41-33\eta)} [1 + (\frac{12}{5} \eta(4\eta-3) + \frac{16}{15\pi} (41-33\eta)) \eta \alpha_s G_0]$	(28)
$\gamma_{\Theta_s} = 12(1-e^2) G_0 \alpha_s^2 \rho_s \sqrt{\frac{\Theta_s}{\pi d_s^2}}$	(29)
$\phi_{\Theta_s} = -3\beta \Theta_s$	(30)
$\eta = 0.5(1+e)$	(31)

equations consist of continuity equations, momentum equations, constitutive relations, and other relations.

In particular, three inter-phase drag models were adopted in this study: the Gidaspow model, the Tang et al. model and the SVFGM model. The Tang et al. model and the SVFGM model have been illustrated in section “Model implementation”, the Gidaspow model was expressed as below⁵:

$$\beta = \begin{cases} 150 \frac{(1-\varepsilon_g)^2 \mu_g}{\varepsilon_g d_s^2} + 1.75 \frac{\rho_g \varepsilon_s |\mathbf{u}_g - \mathbf{u}_s|}{d_s} & (\varepsilon_g \leq 0.8) \\ \frac{3}{4} C_d \frac{\varepsilon_g^{-1.65} \varepsilon_s \rho_g |\mathbf{u}_g - \mathbf{u}_s|}{d_s} & (\varepsilon_g > 0.8) \end{cases} \quad (32)$$

The Gidaspow model, rather than the Tang et al. model was chosen as the primary object for comparison with the SVFGM model, because the drag force calculated from Tang et al. model is greater than that from the Gidaspow model within a specified Re and ϕ_0 . Considering the previous experience of the homogeneous drag model usually overestimated the drag force, it can be expected that a more homogeneous distribution will be obtained from the Tang et al. model. Nevertheless, we also conducted a simulation using the Tang et al. model for the same riser configuration, and the simulation results were nearly consistent with the results obtained from the Gidaspow model.

Riser geometry and simulation parameters

The geometry of the simulated riser was shown in Figure 5. This two-dimensional riser configuration was constructed according to a real CFB experimental rig²⁷ and has been simulated by many researchers previously.^{18–20,28} The inlet and outlet for solid phase were located at the two sides of riser. The solid flow rate at the outlet was detected; meanwhile the same amount of solids was fed back into the riser to maintain the solid inventory as a constant. The fluidized gas inlet was only specified at the bottom of the riser. The grid size was set to 2.25 mm × 2.25 mm for a fine grid and 4.5 mm × 4.5 mm for a not particularly coarse grid. The time step was set to 0.0002 s for all simulations. At the initial time, the particle

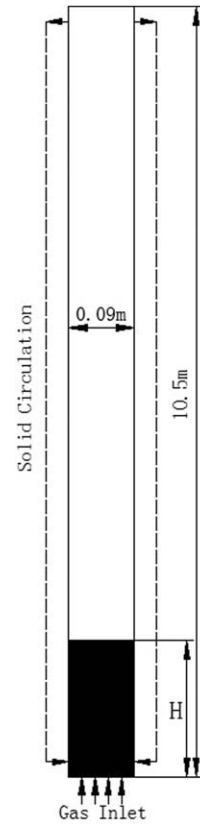


Figure 5. Geometry of the simulated riser.

was stacked up to 1.855 and 1.225 m with voidage of 0.5 for solid inventories of 20 and 15 kg, respectively. The other parameters for the simulation were shown in Table 2.

Flow structure analysis

The solid mass flux obtained from the simulations and the experiment was shown in Figure 6. The instantaneous value within 18 – 30 s was shown because a stable operation in the riser was achieved in all the CFD simulation cases within this period. It was seen that the solid mass fluxes from the Gidaspow model (81.98 kg m⁻²s⁻¹ for solid inventory of 20 kg and 54.82 kg m⁻²s⁻¹ for solid inventory of 15kg) were much higher than these from the SVFGM model (14.14 kg m⁻²s⁻¹ for solid inventory of 20 kg and 12.16 kg m⁻²s⁻¹ for solid inventory of 15 kg). This is because a dilute-top/dense-bottom SVF distribution simulated by the SVFGM model, while only a nearly uniform SVF distribution was obtained in the simulation of the Gidaspow model.

For different solids inventories, it was seen that the solid mass flux increases with the increasing of solid inventory in the simulation of the Gidaspow model, while the solid mass

Table 2. Parameters for the Simulation

Parameter	Value
Particle diameter	54 μm
Particle density	930 kg/m ³
Time interval	0.0002 s
Grid size	2.25 mm, 4.5 mm
Solid inventory	20 kg (1.885 m), 15 kg (1.225 m)
Superficial gas velocity	1.52 m/s

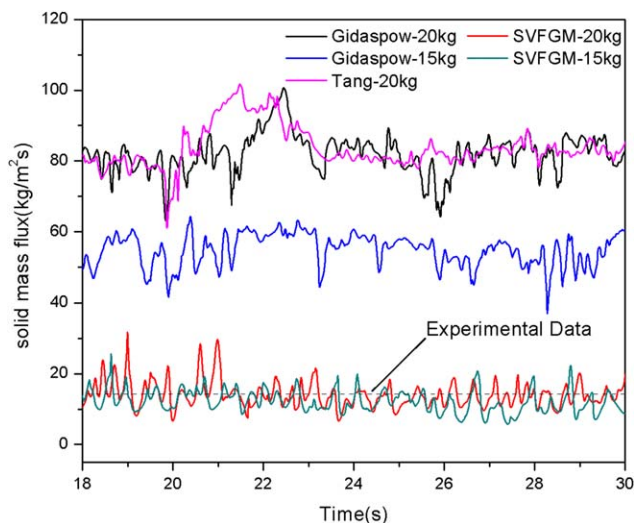


Figure 6. Outlet solid mass flux comparison between the CFD simulations and the experimental measurement.

[Color figure can be viewed at wileyonlinelibrary.com]

flux maintains a lower value in the simulation of the SVFGM model. The reason is that there is a large solid concentration at the riser outlet due to the uniform SVF distribution (in simulation of the Gidaspow model), and the solid concentration increases along with the solids inventory increasing. Additionally, the uniform-distributed particles usually follow the gas more closely. As a result, a large solid mass flux forms and this flux also increases along with the increasing of solids inventory. On the contrary, since there exists a dilute-top/dense-bottom SVF distribution in the riser (in simulation of the SVFGM model), the solid concentration at the riser outlet will maintain a lower value with the increasing of solids inventory, because most of the solid particles were stored on the bottom of the bed. In fact, the entrainment ability of the fluidized gas has reached a maximum value in all the two different solid inventory conditions. However, it was observed

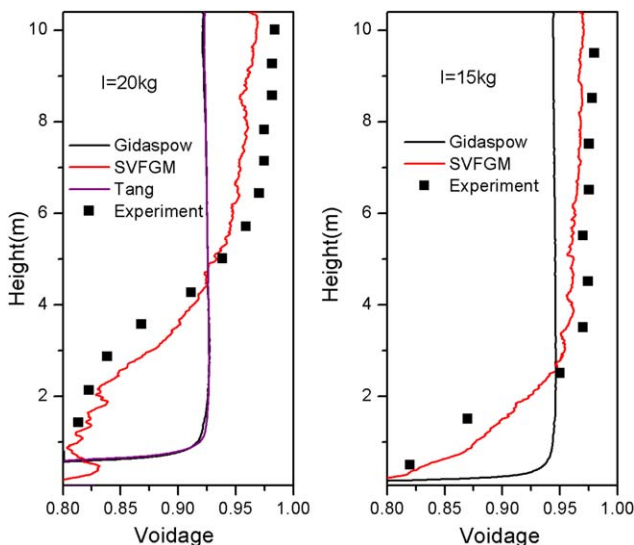


Figure 7. Time-averaged axial voidages (line for CFD simulation and dot for experimental measurement).

[Color figure can be viewed at wileyonlinelibrary.com]

that the height of the dense bed changes as solid inventory (see Figure 7). The above analysis is in accordance with the previous experimental observation,²⁷ and the simulation results from the SVFGM model are in good agreement with the experimental measurements.²⁷

The time-averaged (within 18~30 s) axial voidage results from the simulations and from the experiment conducted by Li and Kwauk²⁷ was shown in Figure 7. Except the inlet region, a nearly uniform axial voidage profile was obtained from the simulation of the Gidaspow model. This phenomenon was also shown in Figure 8. While in the simulation of SVFGM model, the time-averaged axial voidage are in good agreement with the experimental measurements. The exponential voidage profile was transformed into S-shaped voidage profile as the solid inventory increases. Following with this transformation, the height of the dense-bottom-region increases, and the voidage in the dilute-top-region nearly maintains a certain value. The constant voidage in the dilute-top-region results in a constant outlet solid mass flux for different solids inventory conditions.

The instantaneous and time-averaged SVF distributions were shown in Figure 8. The above conclusions (e.g., the S-shaped distribution for axial voidage, the distribution change properties and the constant voidage in the dilute-top-region) can be observed more intuitively. It is worth noting that these figures are compressed along with the axis direction of the riser, and some details looks anamorphic. A local detailed snapshot without compression is shown in Figure 8c. Generally, the slip direction is perpendicular to the direction of SVF gradient, which proved that the first assumption is basically reasonable in this case.

The radial profiles of the time-averaged voidage are shown in Figures 9 and 10. For solid inventory (I) of 15 kg, the height of 1.75 and 4.55 m are located in a typical dense region and in a typical dilute region, respectively, while for I = 20 kg the two values change to 3.5 and 8.75 m. Generally speaking, the results from the SVFGM model are better than the results from the Gidaspow model when compared with the experimental measurements, although there still exist some differences between the simulation results from the SVFGM model and the experimental measurements, especially in the core region. Due to most particles aggregate in the annulus in fast fluidized beds, the under-prediction of the voidage in the core region would have little effect on the accuracy of hydrodynamic simulations.¹⁹ It was considered that these differences were more likely from the inaccurate boundary condition for the particle phase. Shah et al.²⁸ pointed out that the simulation results of radial profile rather than axial profile were more likely affected by the boundary condition for the particle phase. As shown in Figure 7, the difference of axial voidage between simulation results and the experimental measurements is really less than the difference of radial voidage shown in Figures 9 and 10. Therefore, it is reasonable to infer that the boundary condition for the particle phase we chose in our simulations may not accurate enough. In fact, the boundary condition for the particle phase is also under development and far from perfection.

The effect of grid refinement

The SVFGM drag model may be considered as a grid refinement craft by the readership because the main idea of the SVFGM drag model is dividing the computational grid into a dense subgrid and a dilute subgrid. To demonstrate the difference between them, as shown in Figure 11, the instantaneous

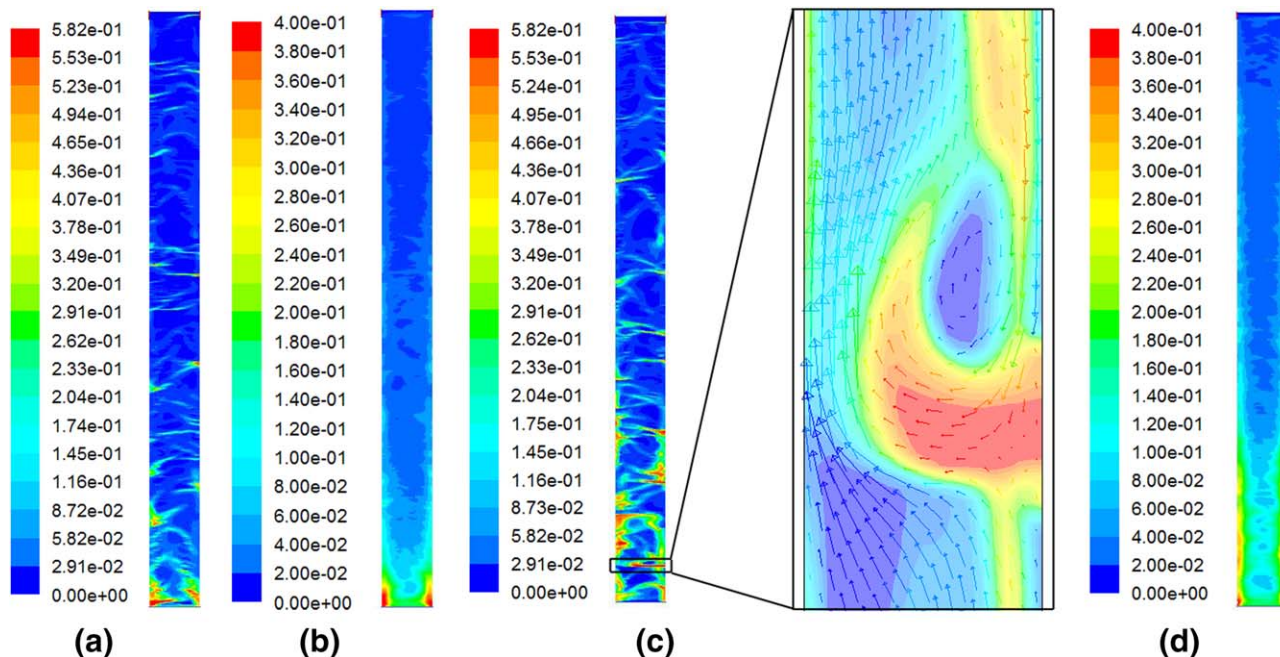


Figure 8. Solid volume fraction distributions from the SVFGM model.

(a) $I = 15$ kg, instantaneous distribution at 30 s (b) $I = 15$ kg, time-averaged distribution (c) $I = 20$ kg, instantaneous distribution at 30 s (d) $I = 20$ kg, time-averaged distribution. [Color figure can be viewed at wileyonlinelibrary.com]

SVF distributions at 30 s with different grid sizes (coarse grid and fine grid) using different drag models (the Gidaspow model and the SVFGM model) were compared. The dilute-top/dense-bottom and dilute-core/dense-wall phenomenon can be observed both in the coarse and fine grid simulation of the SVFGM model, while only a nearly homogeneous distribution can be obtained both in two simulations of the Gidaspow model.

The above comparison illustrated that the prediction improvement of the SVFGM model is not ascribed to the grid refinement (grid size from 4.5 to 2.25 mm in this work). Considering the nonlinear characteristics of the Navier-Stokes equations and the gas–solid interactions, it is not difficult to understand this conclusion. Due to such nonlinear characteristics, dividing the computational grid at different simulation steps (the grid meshing step or the gas–solid drag calculation

step) will lead to different effects on the simulation result. In practice, conceptually dividing the computational grid at the drag calculation step may lead to better simulation results than only refining the computational grid. We also considered that if the computational grid is fine enough, the heterogeneous structure in fast fluidized beds will be captured in CFD simulation of the homogeneous drag models, as demonstrated by Wang et al.²³ and Hong et al.²⁹. However, the computational cost may be unacceptable under this condition. Furthermore, if the grid size has the same order with the particle size, the statistical basis of the TFM may be theoretically false.

Discussion

The concept of the SVF gradient was introduced to deal with the effect of the unresolved structures on the resolved flow. In our modification, the subgrid heterogeneous structures

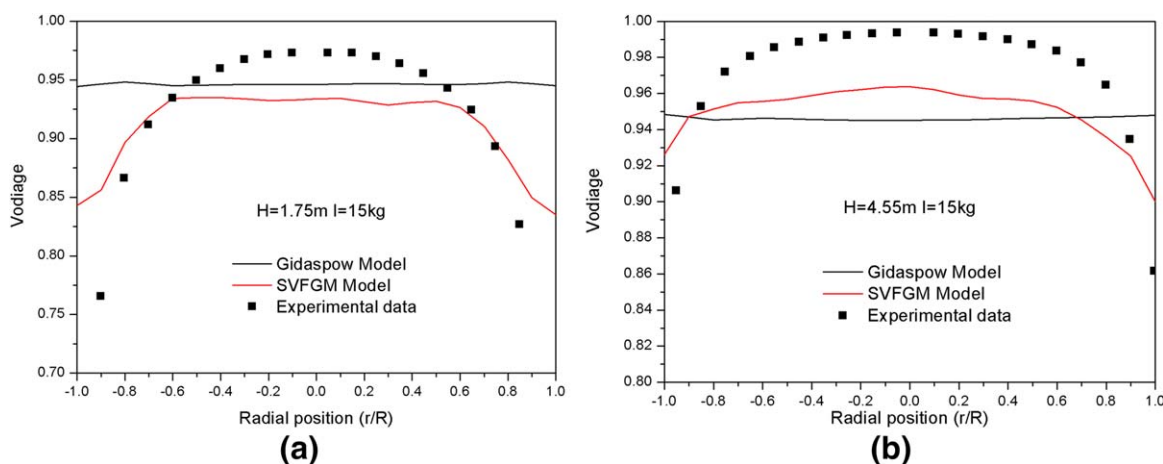


Figure 9. Radial time average voidage profile for $I = 15$ kg.

[Color figure can be viewed at wileyonlinelibrary.com]

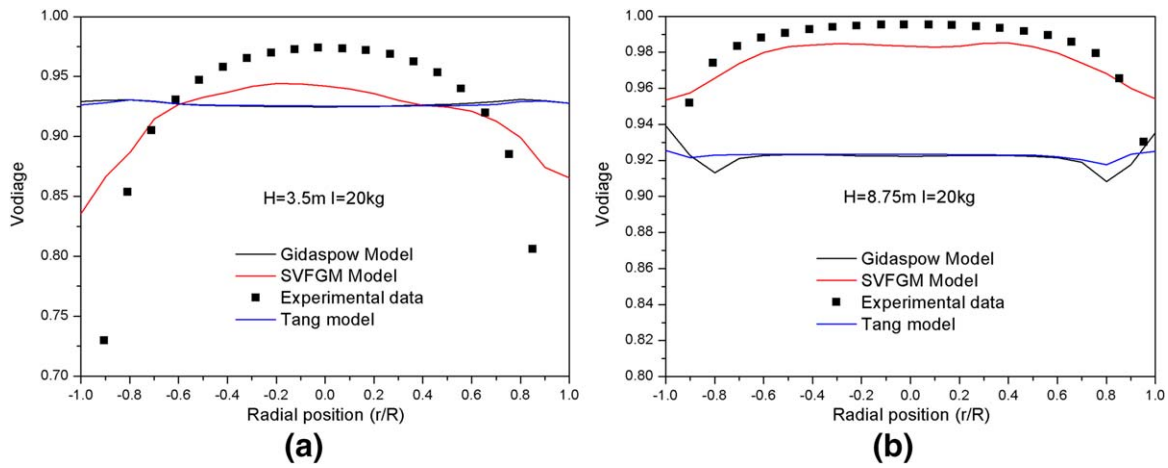


Figure 10. Radial time average voidage profile for $l = 20$ kg.

[Color figure can be viewed at wileyonlinelibrary.com]

named strands (corresponding to the infinite dimensional SVF distribution) were not captured, instead, a subgrid configuration (a dense part and a dilute part) in a computational grid was constructed artificially. By introducing the SVF gradient, a simulation process based on this artificial subgrid configuration can successfully capture the boundary of the cluster under the resolvable scale (in not particularly coarse grid simulations), thus reproducing the cluster phenomenon in the fluidized beds. Although, the present modification looks arbitrary, it conforms to the filtered approach in mathematics and can even be seen as a kind of phenomenological implementation method to the filtered approach. From the perspective of the

cluster formation, the artificial configuration provides the same function to decrease the interphase drag and to maintain the cluster structure as the filtered approach.

The Smagorinsky subgrid model was taken as an inspiration in the present work. However, in large-eddy simulation of turbulent flows the grid size should be restricted to be smaller than the size of the large-scale eddy. Therefore, we recognize that there might be limitation in grid size to the applicability of the SVFGM model. One can envision two types of sub-grid variations in SVF gradient. Type 1: The grid itself is very coarse and the characteristic length scale of the sub-grid scale clusters or bubbles is significantly smaller than the grid size.

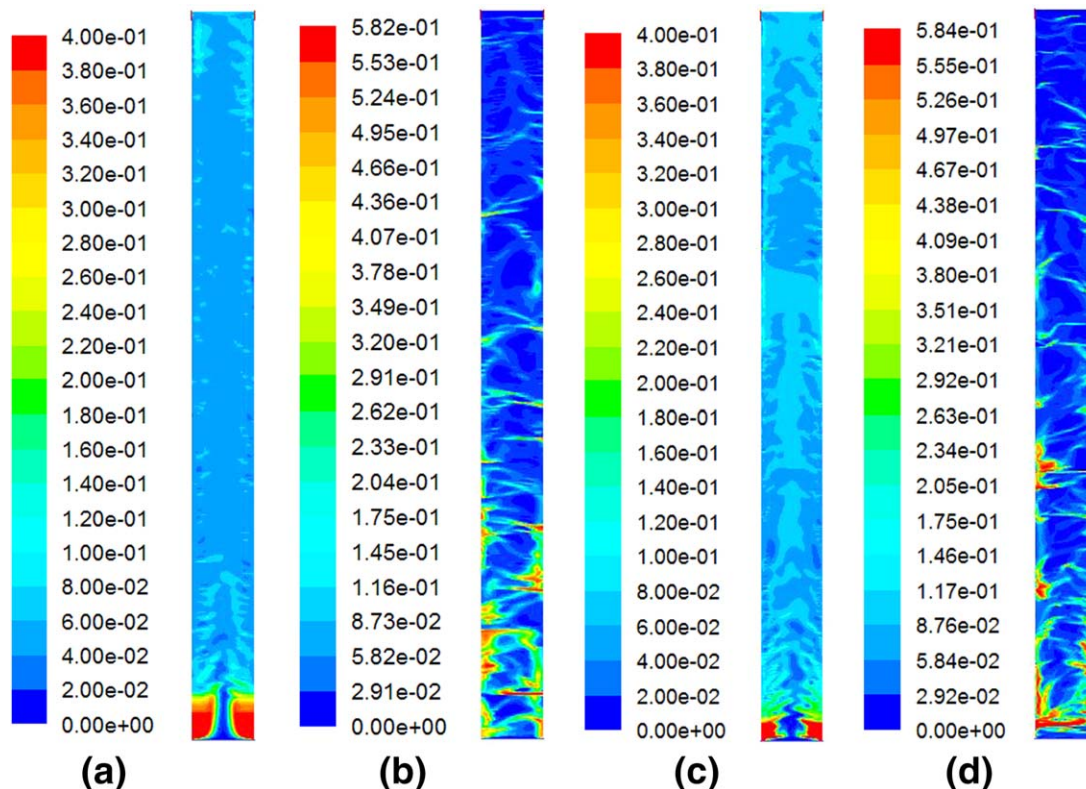


Figure 11. Instantaneous solid volume fraction distribution at 30s (a) Gidaspow model in coarse grid (b) SVFGM model in coarse grid (c) Gidaspow model in fine grid (d) SVFGM model in fine grid.

[Color figure can be viewed at wileyonlinelibrary.com]

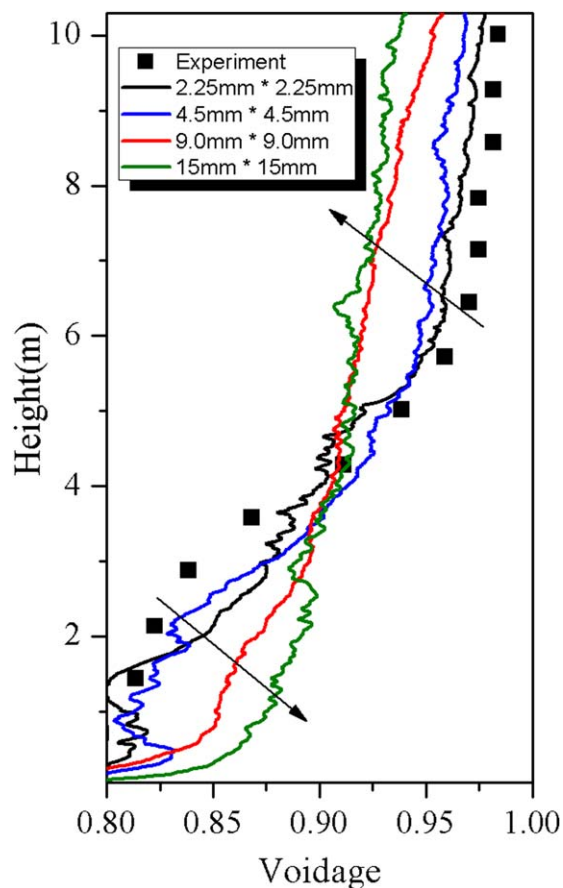


Figure 12. Time-averaged axial voidages with different grid resolutions.

[Color figure can be viewed at wileyonlinelibrary.com]

Type 2: The grid is not particularly coarse and only gently varying SVF gradient exists in the cell. It can be expected that the SVFGM model only works for Type 2. This is because that the SVF gradient calculated from the difference of SVF in two neighboring grids may be different from the actual SVF gradient. More specifically, for Type 2 with “not particularly coarse grids,” the local “resolved” SVF gradient approximates to the actual SVF gradient; however, for Type 1 with “very coarse grids,” the local “resolved” SVF gradient may be far away from the actual gradient. To examine the effect of the grid size on the model adaptability, we conducted another two simulations with particularly coarse grid, and the time-averaged axial voidage results were shown in Figure 12. It can be seen that as the grid size became larger, the solid material distributed more uniformly along with the axis direction, which illustrated that the simulation result with much coarser grids may more deviate from the experimental result. These results verified the above consideration that the present model was only suitable for simulations of not particularly coarse grids.

In the present work, it was assumed that the direction of gas velocity is perpendicular to the direction of the SVF gradient. However, the angle of the two directions may not equal to 90° strictly in practice. The deviation of the real angle from 90° will lead to the difference between the drag force calculated from the present model and its real value. We considered that the drag force should be determined more accurately (by angle correction) in the case of the SVF gradient not perpendicular

to the flow in the future. Factually, at each time step, one can readily calculate the local SVF gradient and the local slip velocity and then obtain the component of SVF gradient in the plane perpendicular to the slip velocity and the component of the SVF gradient aligned with the slip. Then, it is possible to realize the drag correction without the “ 90° ” assumption in theory.

It was also assumed that there is no mass exchange between the two subgrids. This assumption may also lead to some errors. There really exists mass exchange between the two parts in actual processes, especially after taking the above-mentioned angle effect into account. Usually, the flow was not fully developed in the bottom of the cluster; at such position, the mass exchange effect should not be neglected, due to the real angle between the gas velocity direction and the SVF gradient direction deviates from much more than 90° . In the future, particle-resolved direct numerical simulation will be conducted for investigating the drag force for an improved SVFGM drag model.

The SVFGM model can also be improved by increasing the truncation order of $\phi(x)$ based on the Taylor expansion (i.e., by increasing the accuracy of the heterogeneous SVF distribution in a computational grid). In the present work, a computational grid was only divided into two parts conceptually. However, a higher order model may be constructed in the future. At last, we recently noticed that the SVFGM model is consistent with the general form of structure-dependent drag which was proposed by Wang et al.^{30,31} The general form is a function of particle Reynolds number, solid volume fraction, SVF gradient, and the angle between the gradient and the mean slip velocity. In fact, the SVFGM model can be considered as a simplification of the general model. That is, it was assumed that the gradient is perpendicular to the mean slip velocity and the SVF gradient was calculated according to the model assumption (2). In other words, the SVFGM model provides a simple and straightforward realization of the general drag form.

Conclusions

The transient particle clusters forming in risers represent the most typical heterogeneous gas–solid flow structure, leading to a major challenge for both CFD simulation and experimental measurement. In the TFM that has been widely accepted for riser simulation, the key issue to quantify the inherently unstable cluster is to model the inter-phase drag force through considering the effect of the heterogeneous structures on the momentum exchange between the gas and solid phases. The conventional drag model overestimates the drag force, failing in capturing the subgrid-scale strands and resolvable-scale clusters. In the present work, a new inter-phase drag model in which heterogeneous characteristic of SVF distribution in fast fluidized beds was considered for CFD simulation was proposed. The main idea of this work is taking the SVF gradient as an independent variable to modify the drag force calculated from the homogeneous drag correlation. A detailed implementation was proposed based on reasonable assumptions and detailed observation to the heterogeneous phenomenon in fast fluidized beds. Compatibility analysis showed that the presented modification can be seen as a kind of implementation method to the filtered approach. At last, a CFD simulation for a two-dimensional riser was conducted for validating the SVF gradient-modified (SVFGM) drag model. The simulation results were in good agreement with the experimental

measurements. Many experimental observations (e.g., the S-shaped distribution for axial voidage, the distribution change properties and the constant solid mass flux along with the solids inventory changing) were reproduced in the CFD simulation. The SVFGM model, which exhibits clearly theoretical foundations and the advantage of easily programming, provide a promising way to quantify the heterogeneous drag force and capture the meso-scale cluster formation in CFD simulation (with not particularly coarse grids) of fast fluidized beds.

Acknowledgments

This work was financially supported by National Natural Science Foundation of China (51390494 and 51522603). We are also thankful to anonymous reviewers for their useful comments, which illuminated the authors greatly and improved the article substantially.

Notation

d_p = granular diameter, m
 G_0 = radial distribution function
 p = pressure, Pa
 Re = Reynolds number
 e = coefficient of restitution
 \mathbf{g} = acceleration due to gravity, m/s²
 P_s = solid pressure, mol/m³
 \mathbf{u} = velocity vector, m/s

Greek letters

α = voidage
 ϕ = solid volume fraction
 ρ = density, kg/m³
 μ = viscosity, kg/m·s
 σ = stress-strain tensor, Pa
 β = inter-phase drag coefficient, kg/m³s
 $\Delta\phi$ = the solid volume fraction difference between the two parts
 Θ_s = granular temperature
 ζ_s = particle phase bulk viscosity, kg/m·s
 Δ = filter size

Subscripts

g = gas phase
s = particle phase

Superscripts

$\bar{}$ = mean variables after filtering
 \prime = fluctuating variables

Literature Cited

- Li J, Kwauk M. Exploring complex systems in chemical engineering—the multi-scale methodology. *Chem Eng Sci.* 2003;58:521–535.
- Singh RI, Brink A, Hupa M. CFD modeling to study fluidized bed combustion and gasification. *Appl Therm Eng.* 2013;52:585–614.
- Chapman S, Cowling TG. *The Mathematical Theory of Non-Uniform Gases: An Account of the Kinetic Theory of Viscosity, Thermal Conduction and Diffusion in Gases.* Cambridge: Cambridge University Press, 1970.
- Sinclair J, Jackson R. Gas-particle flow in a vertical pipe with particle-particle interactions. *AICHE J.* 1989;35:1473–1486.
- Gidaspow D. *Multiphase Flow and Fluidization: Continuum and Kinetic Theory Descriptions.* San Diego: Academic Press, 1994.
- Hasimoto H. On the periodic fundamental solutions of the Stokes equations and their application to viscous flow past a cubic array of spheres. *J Fluid Mech.* 1959;5:317–328.
- Sangani A, Acrivos A. Slow flow through a periodic array of spheres. *Int J Multiphas Flow.* 1982;8:343–360.
- Wen CY, Yu YH. Mechanics of fluidization. *AICHE J.* 1966;62:100
- Ergun S. Fluid flow through packed columns. *Chem Eng Proc.* 1952;48:89–94.
- Beetstra R, Van der Hoef M, Kuipers J. Drag force of intermediate Reynolds number flow past mono- and bidisperse arrays of spheres. *AICHE J.* 2007;53:489–501.
- Tang Y, Peters E, Kuipers J, Kriebitzsch S, Van der Hoef M. A new drag correlation from fully resolved simulations of flow past mono-disperse static arrays of spheres. *AICHE J.* 2015;61:688–698.
- Li J, Chen A, Yan Z, Xu G, Zhang X. Particle-fluid contacting in circulating fluidized beds. In: Avidan AA, editor. *Preprint Volume for CFB-IV.* New York: AIChE Annual Meeting, 1993:49–54.
- Li J, Wen L, Ge W, Cui H, Ren J. Dissipative structure in concurrent-up gas–solid flow. *Chem Eng Sci.* 1998;53:3367–3379.
- O'Brien TJ, Syamlal M. Particle cluster effects in the numerical simulation of a circulating fluidized bed. In: Avidan AA, editor. *Preprint Volume for CFB-IV.* New York: AIChE Annual Meeting, 1993:430–435.
- Qi H, You C, Boemer A, Renz U. Eulerian simulation of gas–solid two-phase flow in a CFB-riser under consideration of cluster effects. In: Xu D, Mori S, editors. *Fluidization 2000: Science and Technology.* Xi'an: Xi'an Publishing House, 2000:231–237.
- Agrawal K, Loezos PN, Syamlal M, Sundaresan S. The role of meso-scale structures in rapid gas-solid flows. *J Fluid Mech.* 2001;445:151–185.
- Li J, Tung Y, Kwauk M. Multi-scale modeling and method of energy minimization in particle-fluid two-phase flow. In: Basu P, large JF, editors. *Circulating Fluidized Bed Technology II.* Oxford: Pergamon Press, 1988:89–103.
- Yang N, Wang W, Ge W, Li J. CFD simulation of concurrent-up gas–solid flow in circulating fluidized beds with structure-dependent drag coefficient. *Chem Eng J.* 2003;96:71–80.
- Wang J, Ge W, Li J. Eulerian simulation of heterogeneous gas–solid flows in CFB risers: EMMS-based sub-grid scale model with a revised cluster description. *Chem Eng Sci.* 2008;63:1553–1571.
- Lu B, Wang W, Li J. Searching for a mesh-independent sub-grid model for CFD simulation of gas–solid riser flows. *Chem Eng Sci.* 2009;64:3437–3447.
- Shuai W, Huang L, Jianmin G, Huilin L, Guodong L, Pengfei X, Yurong H. CFD simulation of gas–solid flow with a cluster structure-dependent drag coefficient model in circulating fluidized beds. *Appl Math Model.* 2013;37:8179–8202.
- Igci Y, Andrews AT, Sundaresan S, Pannala S, O'Brien T. Filtered two-fluid models for fluidized gas-particle suspensions. *AICHE J.* 2008;54:1431–1448.
- Wang J, Van der Hoef M, Kuipers J. Why the two-fluid model fails to predict the bed expansion characteristics of Geldart A particles in gas-fluidized beds: a tentative answer. *Chem Eng Sci.* 2009;64:622–625.
- Parmentier JF, Simonin O, Delsart O. A functional subgrid drift velocity model for filtered drag prediction in dense fluidized bed. *AICHE J.* 2012;58:1084–1098.
- Smagorinsky J. General circulation experiments with the primitive equations: I. The basic experiment. *Mon Weather Rev.* 1963;91:99–164.
- Zhang MC, Zhang C. A type-A-choking-oriented unified model for fast fluidization dynamics. *Powder Technol.* 2013;241:126–141.
- Li J, Kwauk M. *Particle-Fluid Two-Phase Flow: The Energy-Minimization Multi-Scale Method.* Beijing: Metallurgical Industry Press, 1994.
- Shah MT, Utikar RP, Pareek VK, Tade MO, Evans GM. Effect of closure models on Eulerian–Eulerian gas–solid flow predictions in riser. *Powder Technol.* 2015;269:247–258.
- Hong K, Chen S, Wang W, Li J. Fine-grid two-fluid modeling of fluidization of Geldart A particles. *Powder Technol.* 2016;296:2–16.
- Zhou G, Xiong Q, Wang L, Wang X, Ren X, Ge W. Structure-dependent drag in gas–solid flows studied with direct numerical simulation. *Chem Eng Sci.* 2014;116:9–22.
- Li T, Wang L, Rogers W, Zhou G, Ge W. An approach for drag correction based on the local heterogeneity for gassolid flows. *AICHE J.* 2016; doi:10.1002/aic.15507.

Manuscript received Aug. 8, 2016, and revision received Oct. 27, 2016.